arXiv:1604.04500v3 [cond-mat.mtrl-sci] 2 Jun 2016

Relativistic origin of slow electron-hole recombination in hybrid halide perovskite solar cells

Pooya Azarhoosh, Scott McKechnie, and Mark van Schilfgaarde*

Department of Physics, Kings College London, London WC2R 2LS, UK

Jarvist M. Frost

Centre for Sustainable Chemical Technologies and Department of Chemistry, University of Bath, Claverton Down, Bath BA2 7AY, UK

Aron Walsh

Centre for Sustainable Chemical Technologies and Department of Chemistry, University of Bath, Claverton Down, Bath BA2 7AY, UK and

Global E^3 Institute and Department of Materials Science and Engineering, Yonsei University, Seoul 120-749, Korea

(Dated: June 3, 2016)

Abstract

The hybrid perovskite $CH_3NH_3PbI_3$ (MAPI) exhibits long minority-carrier lifetimes and diffusion lengths. We show that slow recombination originates from a spin-split indirect-gap. Large internal electric fields act on spin-orbit-coupled band extrema, shifting band-edges to inequivalent wavevectors, making the fundamental gap indirect. From a description of photoluminescence within the quasiparticle self-consistent *GW* approximation for MAPI, CdTe and GaAs, we predict carrier lifetime as a function of light intensity and temperature. At operating conditions we find radiative recombination in MAPI is reduced by a factor of more than 350 compared to direct gap behavior. The indirect gap is retained with dynamic disorder.

* Electronic mail:mark.van_schilfgaarde@kcl.ac.uk

Metal-organic perovskite solar cells, $CH_3NH_3PbI_3$ (MAPI) in particular, have attracted much recent attention because of their high power conversion efficiency and potential low cost. The material exhibits strong absorptivity characteristic of a direct-gap semiconductor, with the slow radiative recombination characteristic of an indirect-gap semiconductor. The minority carrier diffusion length considerably exceeds the material thickness required for complete solar capture. As such, internal quantum efficiencies approach 100% [1]. Power conversion efficiencies as high as 21% have been reported[2]. The constituent elements are abundant and efficient devices can be made with solution processing methods which offer the potential for low-cost and large scale production. MAPI is thus perhaps the first competitive realization of a "third generation" solar cell[3].

Minority carrier recombination lifetimes of tens of microseconds are reported in MAPI by time-resolved photoluminescent (TRPL) spectroscopy and other methods [4–6]. Such long lifetimes are found in high-quality samples of crystalline silicon, the archetype indirect-gap semiconductor. A variety of trap-based models have been used to interpret the TRPL data[6, 7]. These models suggest that the long lifetimes are due to immobilisation of charges in traps. However, samples (both single- and poly-crystalline) with trap density differences of the order 10^5 have lifetime variations of only an order of magnitude. This suggests that lifetime is weakly correlated with measured trap density. Further, longer lifetimes are observed in low trap-density single-crystal samples.

We show that the observed slow radiative recombination is an *intrinsic property* of MAPI due to the details of the electronic band structure. We formulate the recombination rate in the framework of the quasiparticle self-consistent GW (QSGW) approximation. A spin-split indirect-gap is formed. Assuming charge carriers thermalize rapidly within a band, we calculate recombination as a function of charge density (illumination intensity) and temperature. With low doping density and solar illumination intensities, the material exhibits an indirect-gap. We show that under operating solar cell conditions, radiative recombination rate is suppressed by over 350 fold; moreover, it varies in an anomalous manner, increasing rapidly with temperature, and illumination intensity and doping. This is in contra-distinction to semiconductors such as CdTe or GaAs, whose recombination properties are also calculated.

For crystals without inversion symmetry, spin-orbit coupling (SOC) splits spin-degenerate levels in non-magnetic systems. In MAPI, significant local electric fields, acting on the large SOC contribution from the heavy lead atom, generate a significant shift in the spin-

degenerate conduction band minimum of Pb $6p$ character. This minimum splits into a pair of minima antipodal to the original point[8], causing the gap to become slightly indirect (Fig. 1). We investigate the effect of dynamic disorder on this spin splitting. Our initial model is a single unit cell, with an infinite array of aligned organic moieties. In reality, the organic moiety rotates on a picosecond timescale at room temperature [9–12]. We sample molecular dynamics realisations of a disordered supercell. In spite of the disorder, the spin-split indirect-gap is not only present but *enhanced*.

The band splitting is a robust property of the material in working solar cells that suppresses radiative recombination of minority charge carriers, enhancing the photovoltaic action. Two recent studies have noted the importance of the formation of an indirect band gap on the recombination rate of MAPI [13, 14]. In Ref. [13], an indirect gap was observed for certain molecular orientations. In Ref. [14], the indirect band gap is recognised as the result of Rashba splitting, leading to a mismatch in both momentum and spin. While their work emphasizes spin-mismatch, we believe that the momentum-mismatch dominates device performance as the valence bands are only slightly split, and geminate recombination is likely to be a minor process.

In this Letter, we report the recombination rate with spin-orbit coupling included in the Hamiltonian, thus directly treating both spin and momentum mismatch. To our knowledge, the only comparable calculation of radiative recombination was by Filipetti et al. where the rate was calculated from density-functional theory without the spin-orbit coupling that is essential for both momentum and spin mismatch.

Above 162 K, MAPI undergoes a continuous transition from a tetragonal to a pseudocubic structure [10]. At room temperature the tetragonal distortion is small, $c/2a \approx 1.01$. The organic moiety in MAPI has a relatively low barrier to rotation [15], and rotates at room temperature in a quasi-random fashion. On average the structure can be considered to be cubic [9–11]. We initially construct a model with a single formula unit of $CH_3NH_3PbI_3$. We orient the organic moiety along [100], [110], and [111], where local potential energy minima are found, which generate three structures representative of the disordered system.

In the absence of spin-orbit coupling the valence band maximum (VBM) and conduction band minimum (CBM) $k_{\min}$ lie at the $\langle 111 \rangle$ R point [8, 16]. The former consists mainly of I $5p$ character, the latter mainly Pb $6p$. The degeneracy of both extrema are split and displaced by spin orbit coupling ($\langle \xi(r) \rangle \, \mathbf{L} \cdot \mathbf{S}$), which originates near the atomic cores where

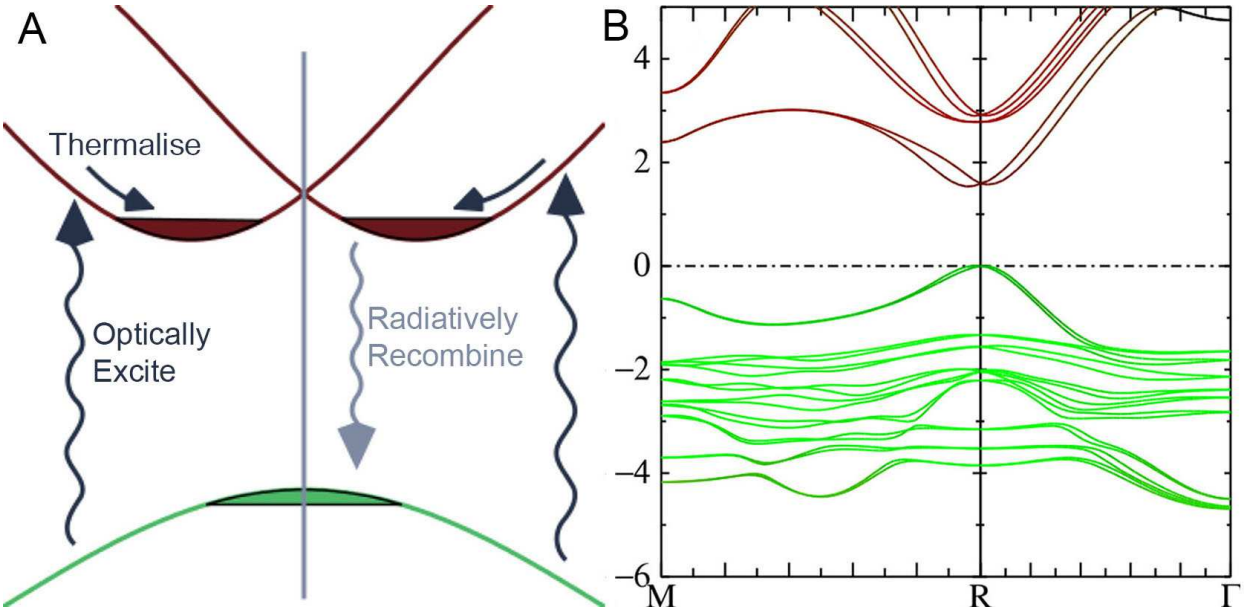

FIG. 1. **Electronic band structure of $CH_3NH_3PbI_3$.** (**A**) schematic of absorption and recombination processes. The conduction bands (red) are split around R, as opposed to conventional direct-gap semiconductors, where there is a single minimum. Photon absorption (dark grey arrows) generate electron-hole pairs, which quickly thermalize to their respective band edges (dark gray arrows) creating a quasi-equilibrium distribution of carriers (red and green). The excess electrons and hole populations can recombine, creating a photon in the process (light grey arrow). Without phonon assist the transitions must be vertical, as shown. If the electron and hole populations are small, the volume of overlapping k space between the red and green distributions becomes exponentially small in $1/k_BT$, while in CdTe and GaAs the two populations occupy the same phase space for any concentration. **(B)** QSGW band structure for a section of the M–R–Γ lines. There is a significant splitting of the conduction band near R (E∼1.75 eV), and a much smaller splitting of the valence band, near (E=0).

$\xi(r)$ is large (Fig. 1). $\langle\xi\rangle$ scales approximately as Z^2.

With Pb being so heavy (Z=82), $\langle\xi\rangle\,\mathbf{L}\cdot\mathbf{S}$ strongly affects the lead $6p$ conduction band, spin-splitting the minima into a pair of distinct states offset from R (Fig. 1). The iodine $5p$ valence band is affected to a lesser extent (Z=53), the spin-split displacement is small, resulting in a flattened region in reciprocal space due to the overlapping minima. The spin-orbit coupling narrows the band gap by ∼1 eV. The spin splitting is linear in k, in contrast

to typical semiconductors where it varies as k^3. The band gap thus becomes slightly indirect. The direct band gap E_0 remains at R, and is 75 meV larger than the indirect gap.

The joint density-of-states (JDOS), relevant for absorption, differs from its direct-gap values in only a small energy range around E_0. The flattened valence band contributes to a large density of states available for optical transition at the direct-gap. Thus *absorption* is only slightly affected by the spin-splitting: MAPI absorbs solar radiation as though it were a direct-gap semiconductor. However, *radiative recombination* is dramatically suppressed. This is extremely unusual for a solar cell material, where typically emission and absorption are the direct reverse of one another. Photoexcited electrons (holes) rapidly thermalize to a small region of k space centered at the conduction (valence) band edges. The asymmetry in $k_{\rm min}^{\rm CBM}$ and $k_{\rm min}^{\rm VBM}$ means that there is a low joint density-of-states of the thermalized minority carriers. Direct (k conserving) recombination is thereby reduced.

Higher temperature leads to greater thermal broadening and a larger overlap in the joint density-of-states, increasing radiative recombination. High density of photogenerated charges (or extrinsic charge carrier doping) fill the small pockets at the CBM. Radiative recombination increases critically, reverting to direct-gap semiconductor behaviour. This property is *intrinsic* to the material; no defect or trap states are needed to explain why radiative recombination is suppressed at low photon flux, but increase dramtically at high photon flux. There is some evidence for such behaviour: carrier lifetimes demonstrate a sharp fall at moderate injection densities [7].

Here we formulate an *ab initio* theory for radiative recombination within the QSGW approximation[17]. QSGW is parameter-free. In *sp* semiconductors a wide range of electronic properties are uniformly well described [18], including splitting from the Dresselhaus terms [19]. Few fully *ab initio* formulations of radiative recombination have been reported[20]. Calculations using the van Roosbroeck-Shockley relation with experimental[21] and theoretical[22] absorption coefficients have been published. We directly calculate the recombination rate without model parameters, adapting the standard theory of dielectric response to non-equilibrium carrier populations.

The recombination dynamics of carriers within the bulk of an intrinsic semiconductor (n=p) can often be accurately described by a third-order rate equation:

$$\frac{dn}{dt} = G - n\mathsf{A} - n^2\mathsf{B} - n^3\mathsf{C} \tag{1}$$

Here n is the density of excited carriers and G is a source term describing constant photogeneration of carriers[23]. These parameters are often fit to experimental transient data across a large range of laser fluences and thus carrier densities[24]. An implicit assumption is that these coefficients do not vary across the carrier density regime experimentally accessed. A is related to the one-body non-radiative carrier recombination, which proceeds through crystal defect levels as intermediate states. We are concerned with intrinsic recombination and do not consider this extrinsic process. C is the three-body Auger recombination coefficient. This has been calculated in a GW framework [25] but it becomes important under strongly non-equilibrium carrier populations and we omit it here. The two-body coefficient B describes radiative recombination of free carriers and is intimately connected with both absorption and emission. Photo-generated carriers thermalize to the band edges on a picosecond time scale [26], which is fast compared to the radiative recombination time (ns to μs).

We will assume that photoexcited carriers thermalize instantaneously within a band to form quasi-equilibrium Fermi-Dirac distributions of electrons and holes. Thus the occupation probability of an excited electron c is given by $f_c = \left(\exp[(E_c - E_c^F)/k_B T] - 1\right)^{-1}$, where $E_c - E_c^F$ is the excitation energy relative to the electron quasi-Fermi level. The corresponding distribution f_v for excited holes is the same form, substituting $E_c - E_c^F \to E_v - E_v^F$. In practice, we specify T, and electron and hole populations n and p. From the QSGW band structure we can calculate the density of states and so determine E_c^F and E_v^F from n and p.

To establish that QSGW can reliably predict the photoluminescent process, we compute B for the benchmark materials GaAs and CdTe. This both validates the method developed here and serves as points of comparison to MAPI.

Under solar intensities a small population of electrons (holes) is excited to the conduction (valence) band (Fig. 1). This density is relatively small for an operating solar cell ($\sim 10^{17}$ cm^{-3}). Only a small area of k space near the band edges is utilized by photo-excited charge carriers. Numerically, this necessitates a fine k mesh to adequately sample the near regions of the band minima. Some additional modest approximations are necessary to make the calculation tractable. We neglect local fields and use the independent-particle (time-dependent Hartree) approximation. This approximation misses the Wannier excitons below

the band edge, but they are very shallow [27, 28]. If the potential is local,

$$\epsilon(\omega) = \sum_{\mathbf{k}cv} \epsilon_{\mathbf{k}cv}(\omega) \tag{2}$$

$$\mathrm{Im}\,\epsilon_{\mathbf{k}cv}(\omega) = \frac{1}{\hbar}\left(\frac{2\pi e}{m\omega}\right)^2 |P_{\mathbf{k}cv}|^2 f_c(1-f_v)\delta(\omega-\omega_{\mathbf{k}cv}) \tag{3}$$

$\epsilon_{\mathbf{k}cv}$ resolves ϵ into individual electron-hole excitations between Bloch states v and c; $\hbar\omega_{\mathbf{k}cv}{=}E_c(\mathbf{k}){-}E_v(\mathbf{k})$ is the excitation energy of the cv pair. The photons couple c to v, which for direct transitions simplifies to a matrix element of the momentum operator $P_{\mathbf{k}cv}$. We omit phonon-assisted indirect transitions that do not conserve k because they are weaker, higher-order processes. As written Eq. (3) is approximate because the QSGW potential is non-local. However, for transitions close to E_0 the effect of non-locality can be described by a scaling of $P_{\mathbf{k}cv}$ [29]. Further details of the theory are given in the supplemental material [30].

By resolving $\mathrm{Im}\,\epsilon$ into individual pair contributions, the transition rate (Einstein coefficient) $A_{\mathbf{k}cv}$ between a cv pair can be readily identified

$$A_{\mathbf{k}cv} = \frac{n_r e^2 \omega_{\mathbf{k}cv} |P_{\mathbf{k}cv}|^2}{\pi\epsilon_0 \hbar c^3 m^2} \tag{4}$$

and the energy-resolved radiative recombination rate is

$$R_{\mathbf{k}cv}(\omega) = f_c(1-f_v)A_{\mathbf{k}cv}\delta[\omega-\omega_{\mathbf{k}cv}] \tag{5}$$

The total emission rate

$$R^{\mathrm{tot}} = \int_0^\infty d\omega \sum_{\mathbf{k}cv} R_{\mathbf{k}cv}(\omega) \tag{6}$$

is conventionally expressed in terms of a carrier density independent recombination lifetime τ or a B coefficient:

$$\tau^{-1} = \mathrm{B}n = R^{\mathrm{tot}}/n. \tag{7}$$

We neglect the scattering processes that eventually lead to thermalizstion of electrons (holes) during photoluminescence. We adopt the standard approximation in device modeling, and assume that recombination is slow compared to the scattering of charge carriers within a band, so a quasi-equilibrium Fermi-Dirac distrbution is maintained with a well-defined, band-dependent chemical potential.

B, computed as a function of carrier density for MAPI, CdTe and GaAs at several temperatures, is shown in Fig. 2. Measured values at room temperature are displayed in Table

I. These vary widely, presumably owing to the competition of B with other, non-radiative, recombination paths. The presence of these pathways will depend strongly on how the material is fabricated, and so the smallest measured B value is probably the most reliable, and the most directly comparable to our calculations. We calculate B to be more than two orders of magnitude smaller in MAPI than the direct-gap semiconductors CdTe and GaAs, but larger than the fully indirect Si. MAPI resembles an indirect gap semiconductor for radiative carrier recombination, and a direct gap semiconductor for absorption.

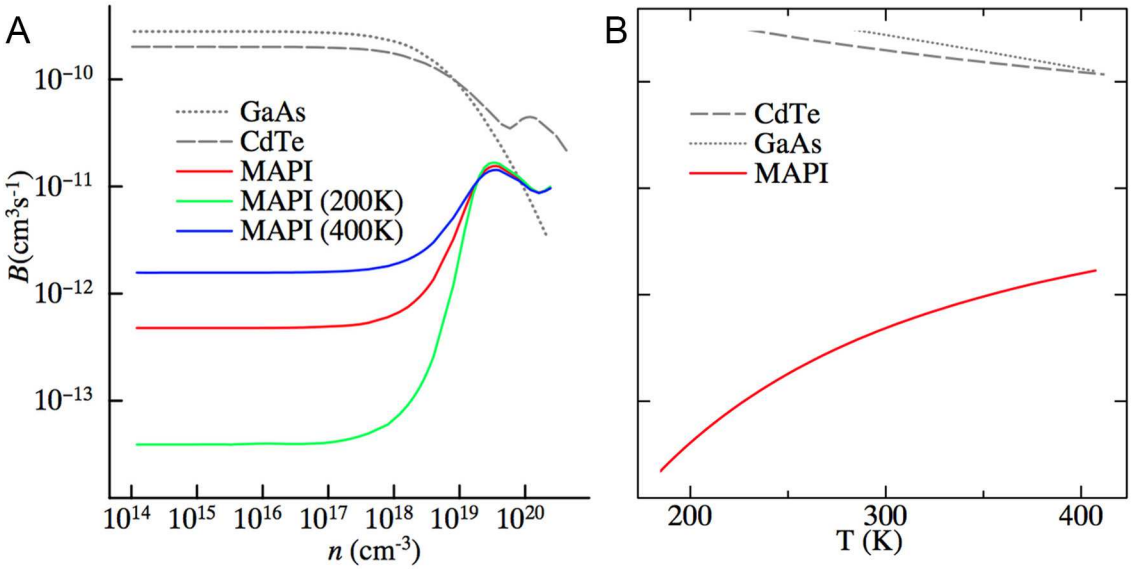

FIG. 2. **Radiative recombination coefficient for varying temperature and excitation intensity.** **(A)** Radiative recombination coefficient B in the intrinsic case n=p. Left: B for CdTe, GaAs and MAPI at room temperature, varying photoexcitation density n. All have comparable direct band gaps and effective masses. At n>10^{18}cm^{-3} the MAPI spin-split indirect-gap saturates and the rate of radiative recombination becomes similar in all three materials. Also shown are MAPI calculated at 200 K and 400 K. The effect of the indirect gap becomes more pronounced as T decreases. **(B)** Temperature dependence of radiative recombination for n=10^{16} cm^{-3}.

The magnitude of B increases as the k-space overlap between electron and hole distributions increases. This causes the rate of bimolecular recombination to depend on external parameters in an unusual manner. For example, increasing temperature smears f_c and f_v over a wider band of k for fixed n, causing B to increase with T. The temperature dependence of B in GaAs and CdTe (Fig. 2) is weaker and of opposite sign. Further, bimolecular

recombination will increase abruptly with photoexcited carrier density once the electon pockets begin to fill up and overlap ($n{\sim}10^{18}\mathrm{cm}^3\mathrm{s}^{-1}$ in Fig. 2), in sharp contrast to CdTe and GaAs. Only at high carrier concentrations when a significant fraction of electrons and holes overlap does B in MAPI become comparable to B in CdTe, where it also adopts the conventional behaviour and begins to decrease with increasing n. The strong carrier density, and therefore laser-fluence, dependence of B suggests that global fits to time resolved data are not a reliable method to infer B or lifetime from B (equation 7). The variation of B with carrier density will make high fluence transients multi-exponential, and break the expected relationship between light-emission and carrier-density sensitive experimental probes.

For photoexcitation densities $n{<}10^{17}\mathrm{cm}^3\mathrm{s}^{-1}$ ($n{=}p$), we find $\mathrm{B} \approx 4{\times}10^{-13}$ at room temperature. These are the charge carrier densities relevant for device operation in sunlight. As B is fairly constant below this charge carrier density, we can use equation 7 to derive a lifetime of order 10-100 μs. This lifetime is consistent with values reported in literature for single crystal samples under 1 and 0.1 sun intensity[4–6].

There is limited temperature dependent TRPL data available. Most data is for polycrystalline films, whereas our results would best be compared to single crystal measurements. Yet it has been observed that the carrier lifetime is highly temperature sensitive at low fluence while being temperature insensitive at high fluence [6]. The increase in minority carrier lifetime with decreasing sample temperature can be directly explained by a contraction of the Fermi-Dirac distribution near the spin-split band minima.

So far we have considered MAPI in an idealized static structure. In reality, the high temperature phase of MAPI is cubic on average only; the dipolar molecules between cages continually rotate, the cages flex and tilt. Second-order Jahn-Teller deformations of the octahedra due to the Pb 6s lone pair directly distort the lead iodide bonds, generating local electric fields near the atomic core region where spin-orbit coupling is high. Recent molecular-dynamics simulations by Etienne et al. [31] suggest that the conduction band splitting persists in the presence of disorder.

If the material has true inversion symmetry, as MAPI is believed to in the orthorhombic phase below 162 K, no directional electric fields can exist, and so the spin-split indirect-gap should vanish. The rate of radiative recombination should increase, increasing the competition with non-radiative recombination and thus increasing photoluminescent efficiency.

To assess the effect of dynamic disorder we performed *ab-initio* molecular dynamics at 300

K with a 2×2×2 supercell. Such supercells are able to accurately describe the phonon modes both at the Γ point and the Brillouin zone boundary; these k-points contain the important low-energy vibrational modes responsible for disorder. We extract 100 realisations, each temporally separated by 0.25 ps, collected after an initial equilibration period. Given the increased computational cost of this larger structure (96 versus 12 atoms), the electronic properties were calculated within the local density approximation (LDA) including spin-orbit coupling. While our intent is to show the qualitative effect of disorder on the magnitude of the spin-split indirect-gap and the effective masses, the LDA results for the ordered cells are in reasonable agreement with QSGW (Table II).

Between molecular dynamics snapshots, the spin-split band extrema and effective masses fluctuate. As can be seen from values averaged over the 100 instances (table II), disorder causes the light effective masses to increase. This may explain the observed reduction in mobility as a function of temperature, in the temperature regime where the organic moieties are increasingly disordered. Surprisingly, the band minima spin-split $k_{\min}$ *also* increases with disorder. This suggests that the cage deformation plays a more important role in generating the directional electric field than the ordering of the moiety dipoles. This is indirectly supported by the success of the formamidinium based perovskites, with smaller dipoles but larger anisotropy [32, 33].

Although the model presented here shows good agreement with experiment, other mechanisms that suppress bimolecular recombination may be operative. In particular, electric fields generated by local ferroelectric domains or defect segregation could separate electrons and holes in *real* space [15, 34], in contrast to the present work, where B is suppressed by separation in *reciprocal* space. Both mechanisms could contribute simultaneously to reduced recombination. We pointed to a limited body of evidence to support the latter; along these lines it is noteworthy that high power conversion efficiencies have been reported only for lead-based halide perovskites. This is consistent with the spin-split indirect-gap picture, as SOC is weaker in lighter elements such as Sn. In principle it is possible to obtain experimental evidence for the direct/indirect-gap picture, with optical probes of the (weakly emissive) indirect gap. Sensitive photoluminescence (PL) or electroluminescence (EL) would probe the emission from this state, absorption can be probed by sensitive external quantum efficiency (EQE) or photo-deflection spectroscopy (PDS). In our idealized structure we predict the splitting to be 75 meV, while in the actual, disordered case it will vary with the disorder.

Thus we expect the splitting to decrease with temperature.

In summary we have provided a fully *ab initio* relativistic calculation of the hybrid halide perovskite radiative recombination lifetime. We considered only direct recombination, and with electron and hole populations described by a quasi-Fermi level. We have shown that the bimolecular recombination rate is strongly temperature and carrier density sensitive, and that the long carrier lifetime and diffusion length are a direct consequence of large relativistic spin-orbit coupling combined with internal electric fields. We suggest that the relevant electric fields are mainly generated by dynamic deformation of the inorganic octahedral cage. The spin-split indirect-gap is generated by the Pb lone-pair driven distortions, and the Pb spin-orbit coupling of the conduction band. For perovskite alloys, for example formamidinium/methylammonium/caesium and iodine/bromine, the additional symmetry breaking due to occupational site disorder would be expected to further enhance these effects, which is consistent with their strong photovoltaic action.

ACKNOWLEDGMENTS

The authors thank Jenny Nelson, Thomas Kirchartz and Keith Butler for useful discussions. The research has been supported by the EPSRC (Grant Nos. EP/K016288/1, EP/M009580/1 and EP/M009602/1), the Royal Society, and the European Research Council (No. 277757). Computational resources were provided by the University of Bath, and the EPSRC (Grant No. EP/L000202).

	Expt (10^{-12}cm^3-s^{-1})	QSGW
MAPI	see text	0.49
GaAs[35–37]	130–1300	267
CdTe[38–40]	100–5100	195
Si[41, 42]	0.001–0.01	

TABLE I. Experimental and QSGW values for B at room temperature, and n=10^{17}cm^{-3}.

Structure	Theory	k_{min} (Å^{-1})	m_1	m_2	m_3
Pseudocubic ⟨100⟩	QSGW	0.043	0.95	0.13	0.11
Pseudocubic ⟨110⟩		0.055	0.13	0.11	0.11
Pseudocubic ⟨111⟩		0.043	0.36	0.12	0.12
Pseudocubic ⟨100⟩	LDA	0.049	1.03	0.09	0.06
Pseudocubic ⟨110⟩		0.057	0.08	0.07	0.06
Pseudocubic ⟨111⟩		0.049	0.27	0.08	0.08
Molecular Dynamics		0.105	1.02	0.60	0.42

TABLE II. Calculated values of $k_{\min}$ and conduction band effective masses along the three principal axes. LDA results for the molecular dynamics 2×2×2 supercell are the average from one hundred snapshots.

I. SUPPLEMENTAL MATERIAL

A. Recombination Rate

Considering first order perturbation theory for the spontaneous emission from a two state system, the Einstein A coefficient is given by

$$A_{cv}(\omega_{cv}) = \frac{n_r e^2 \omega_{cv} |P_{cv}|^2}{\pi \epsilon_0 \hbar c^3 m^2} \delta(E_c - E_v - \hbar\omega_{cv}) \tag{S1}$$

Here $|P_{cv}|$ is the matrix element for this transition. The states are labelled c and v in anticipation of these states referring to conduction and valence bands of a periodic material.

Considering the continuum response of a medium, the imaginary component of the dielectric function can be defined as

$$\epsilon_i^{cv} = (2\pi e)^2 \sum_{\vec{k}} |P_{cv}|^2 \delta(E_c(\vec{k}) - E_v(\vec{v}) - \hbar\omega) \tag{S2}$$

This can be directly related to the absorption through $\sigma(\omega) = \frac{4\pi\kappa(\omega)}{\lambda} = \frac{2\pi\epsilon(\omega)}{n_r \lambda}$. Rearranging the momentum matrix element P_{cv} and substituting into the imaginary component of the dielectric function, we can express the imaginary component of the dielectric function as a sum over Einstein coefficients[43]

$$\epsilon_i^{cv}(\omega_{cv}) \frac{\omega_{cv}^3 n_r}{4\pi\epsilon_0 \pi^2 c^3 \hbar} f_c(1 - f_v) = \sum_k A_{cv}\, \delta[E_v(k) - E_c(k) - \hbar\omega_{cv}] \tag{S3}$$

Integrating over all transition energies, we get the total rate of transition per unit volume for all direct transitions, such that:

$$R_{cv}^{Tot} = \frac{n_r}{4\pi^3 c^3 \hbar^4 \epsilon_0} \int_0^\infty dE \epsilon_i^{cv}(E_{cv}) E_{cv}^3 = \int_0^\infty dE \sum_k A_{cv} \delta[E_v(k) - E_c(k) - \hbar\omega_{cv}] \tag{S4}$$

In the limit of non density dependence, this quantity is related to the radiative recombination coefficient B and lifetime through

$$\tau^{-1} = nB = \frac{R_{cv}^{Tot}}{n} \tag{S5}$$

In this work we directly evaluate R_{cv}^{Tot} by Expression S4 as we have direct access to the microscopic optical matrix elements and imaginary part of the dielectric function.

This equation is equivalent to the van Roosbreck-Shockley formalism. This correspondence we will now show.

We start by rewriting Equation S3 in terms of the absorption coefficient

$$\sigma(\omega)\frac{n_r\lambda}{2\pi}\frac{\omega_{cv}^3 n_r}{4\pi\epsilon_0\pi^2c^3\hbar}f_c(1-f_v) = \sum_k A_{cv}\,\delta[E_v(k)-E_c(k)-\hbar\omega_{cv}] \tag{S6}$$

$$\sigma(\omega)\frac{[\hbar\omega_{cv}]^2 n_r^2}{4\pi^3\epsilon_0c^2\hbar^3}f_c(1-f_v) = \sum_k A_{cv}\,\delta[E_v(k)-E_c(k)-\hbar\omega_{cv}] \tag{S7}$$

Converting to cgs units we get the simplified expression

$$\sigma(\omega)\frac{[\hbar\omega_{cv}]^2 n_r^2}{\pi^2c^2\hbar^3}f_c(1-f_v) = \sum_k A_{cv}\,\delta[E_v(k)-E_c(k)-\hbar\omega_{cv}] \tag{S8}$$

If we integrate over all frequency and reciprocal space this equation is equivalent to the van Roosbreck-Shockley (vRS) relation. The equivalence can be seen through the definition of the absorption coefficient. In this work we use an absorption coefficient for an athermal system with completely empty conduction bands and completely full valence bands. However one can define an absorption coefficient containing the thermal excitation of charge carriers. This absorption coefficient $\alpha(\omega)$ is given by

$$\alpha_i^{cv}(\omega_{cv}) = \frac{2\pi}{n\lambda}\left(\frac{2\pi e}{m\omega_{cv}}\right)^2\sum_{\vec{k}}|P_{cv}|^2\,(f_c-f_v)\delta(E_c(\vec{k})-E_v(\vec{k})-\hbar\omega) \tag{S9}$$

The Fermi functions in Equation S9 take into account stimulated emission and absorption. These two absorption coefficients are directly related through $\sigma(\omega) = \frac{\alpha(\omega)}{(f_c-f_v)}$. We substitute this form into Equation S8 to arrive at

$$\alpha(\omega)\frac{[\hbar\omega_{cv}]^2 n_r^2}{\pi^2c^2\hbar^3}\frac{f_c(1-f_v)}{(f_c-f_v)} = \sum_k A_{cv}\,\delta[E_v(k)-E_c(k)-\hbar\omega_{cv}] \tag{S10}$$

$$\frac{[\hbar\omega_{cv}]^2 n_r^2}{\pi^2c^2\hbar^3}\alpha(\omega)\frac{1}{\exp(\hbar\omega/k_BT)-1} = \sum_k A_{cv}\,\delta[E_v(k)-E_c(k)-\hbar\omega_{cv}] \tag{S11}$$

This is the conventional form of the van Roosbreck-Shockley relation, hence showing the equivalence of Equation S8 and S11.

Our microscopic model for recombination formally agrees with the macroscopic van Roosbreck-Shockley relation, in the limit where the photon bath within the material is small, and so stimulated emission and absorption processes can be neglected.

B. Effective optical matrix

The imaginary part of the dielectric function is shown in equation S2. We can express the optical matrix element P_{cv} in the momentum gauge as

$$P_{cv}^{Loc} = \frac{-i}{m\,\omega} \langle \psi_{c,\vec{k}} |\, \hat{e} \cdot \vec{p} \,| \psi_{v,\vec{k}} \rangle \tag{S12}$$

This form has the advantage of taking $\lim_{q\to 0}$ analytically. In the length gauge form

$$P_{cv}^{Loc} = \lim_{q\to 0} \frac{1}{q} \langle \psi_{c,\vec{k}+\vec{q}} | \exp(iq\hat{e}\cdot\vec{r}) \,| \psi_{v,\vec{k}} \rangle \tag{S13}$$

the limit persists and must be taken numerically. Both these forms are equivalent. Formally, these are valid only for local Hamiltonians.

This limitation can be overcome by scaling the matrix element by

$$P_{cv} = P_{cv}^{Loc} S^* = P_{cv}^{Loc} \frac{E_c^* - E_v^*}{E_c^0 - E_v^0} \tag{S14}$$

where E_c^* and E_v^* are the eigenvalues of the non-local Hamiltonian for the conduction and valence band respectively, while E_c^0 and E_v^0 are the local Hamiltonian counter parts.
The derivation of expression S14 is outlined below:

$$\lim_{q\to 0} \frac{1}{q} \langle \psi^*{}_c, \vec{k}+\vec{q} | \exp(i\vec{q}\cdot\vec{r}) \,| \psi^*_{v,\vec{k}} \rangle = \lim_{q\to 0} \frac{1}{q} \langle \psi_c^* \,| \psi_c^0 \rangle \langle \psi_v^0 | \,| \psi_v^* \rangle \langle \psi^0_{c\cdot\vec{k}+\vec{q}} | \exp(i\vec{q}\cdot\vec{r}) \,| \psi^0_{v,\vec{k}} \rangle \tag{S15}$$

$$= \frac{1}{m} \langle \psi_c^* | \,| \psi_c^0 \rangle \langle \psi_v^* | \,| \psi_v^0 \rangle \frac{\langle \psi_c^0 |\, \hat{e}\cdot\vec{p} \,| \psi_v^0 \rangle}{E_c^0 - E_v^0} \tag{S16}$$

$$= \frac{1}{m} \langle \psi_c^* | \,| \psi_c^0 \rangle \langle \psi_v^* | \,| \psi_v^0 \rangle \frac{\langle \psi_c^0 |\, \hat{e}\cdot\vec{p} \,| \psi_v^0 \rangle}{E_c^* - E_v^*} \frac{E_c^* - E_v^*}{E_c^0 - E_v^0} \tag{S17}$$

$$= \frac{1}{m} \langle \psi_c^* | \,| \psi_c^0 \rangle \langle \psi_v^* | \,| \psi_v^0 \rangle \frac{\langle \psi_c^0 |\, \hat{e}\cdot\vec{p} \,| \psi_v^0 \rangle}{E_c^* - E_v^*} S^* = |P_{cv}^*| \tag{S18}$$

In the derivation above the asterixed symbols correspond to eigenfunctions ($\langle \psi_c^* |\,, \langle \psi_c^* |$) and eigenenergies ($E_c^*$,$E_v^*$) of a non-local Hamiltonian. This approximation is based on the assumption that the local and non-local eigen functions are almost identical. Using this approximation the imaginary part of the dielectric function can be approximated by

$$\epsilon_i^{cv} = \left(\frac{2\pi e}{m\omega}\right)^2 \sum_{\vec{k}} |P_{cv}^*|^2 \,\delta(E_c(\vec{k}) - E_v(\vec{v}) - \hbar\omega) \tag{S19}$$

This effective optical matrix has been developed by Sole and Girlanda[29], and Levine and Allan[44] independently. We note that this approximation has no qualitative and little

quantitative effect on the central results of the paper. The long carrier lifetimes we predict are mainly due to the unusual joint density of states calculated for these materials due to the spin-split indirect-gap.

C. Computational procedure

All calculations in this report were preformed using the LMSUITE codes[45], which implement an all-electron numeric solution of the quasi-particle self-consistent GW approximation and the improved tetrahedron method as formulated by Blöchl *et al.*[46]. The crystal structures used were energy minimised with the PBEsol[47] functional as implemented in the VASP codes[48]. They are as previously reported[8], and are available in computer readable form [49]. The *QS*GW band structures were calculated on a $120 \times 120 \times 120$ k-mesh. With this high resolution the quasi-Fermi levels are sampled with sufficient accuracy. The partial densities of state were calculated for a given temperature and carrier population with

$$n_c(E) = D(E)f(E,T) \tag{S20}$$

where $n_c(E)$ is the carrier population, $D(E)$ is the density of states and $f(E,T)$ is the Fermi-Dirac function at a given energy and temperature. This assumes the full thermalisation of electrons and holes.

The optical properties and emission spectrum are calculated using the methods described in sections I A and I B and the original main text of the article. For emission calculations only the lowest two conduction and highest two valence bands are taken into account. An energy mesh of 3000 points was used between E_g and $E_g + 3.4$ eV for emission spectrum calculations. This limit covered all emission, and was found to have sufficient mesh fineness for the lowest carrier densities calculated.

---

[1] Q. Lin, A. Armin, R. C. R. Nagiri, P. L. Burn, and P. Meredith, Nature Photon. **9**, 106 (2015).

[2] H. Zhou, Q. Chen, G. Li, S. Luo, T.-b. Song, H.-S. Duan, Z. Hong, J. You, Y. Liu, and Y. Yang, Science **345**, 542 (2014).

[3] M. Green, *Solar cells: operating principles, technology, and system applications*, Prentice-Hall series in solid state physical electronics (Prentice-Hall, 1982).

[4] Q. Dong, Y. Fang, Y. Shao, P. Mulligan, J. Qiu, L. Cao, and J. Huang, Science **347**, 967 (2015).

[5] D. Shi, V. Adinolfi, R. Comin, M. Yuan, E. Alarousu, A. Buin, Y. Chen, S. Hoogland, A. Rothenberger, K. Katsiev, Y. Losovyj, X. Zhang, P. A. Dowben, O. F. Mohammed, E. H. Sargent, and O. M. Bakr, Science **347**, 519 (2015).

[6] S. D. Stranks, V. M. Burlakov, T. Leijtens, J. M. Ball, A. Goriely, and H. J. Snaith, Phys. Rev. Appl. **2**, 034007 (2014).

[7] Y. Yamada, T. Nakamura, M. Endo, A. Wakamiya, and Y. Kanemitsu, J. Am. Chem. Soc. **136**, 11610 (2014).

[8] F. Brivio, K. T. Butler, A. Walsh, and M. van Schilfgaarde, Phys. Rev. B **89**, 155204 (2014).

[9] E. Mosconi, C. Quarti, T. Ivanovska, G. Ruani, and F. De Angelis, Phys. Chem. Chem. Phys. **16**, 16137 (2014).

[10] M. T. Weller, O. J. Weber, P. F. Henry, A. M. Di Pumpo, and T. C. Hansen, Chem. Commun. **51**, 4180 (2015).

[11] A. M. A. Leguy, J. M. Frost, A. P. McMahon, V. G. Sakai, W. Kockelmann, C. Law, X. Li, F. Foglia, A. Walsh, B. C. O'Regan, J. Nelson, J. T. Cabral, and P. R. F. Barnes, Nat. Commun. **6**, 7124 (2015).

[12] A. A. Bakulin, O. Selig, H. J. Bakker, Y. L. Rezus, C. Mller, T. Glaser, R. Lovrincic, Z. Sun, Z. Chen, A. Walsh, J. M. Frost, and T. L. C. Jansen, J. Phys. Chem. Lett. **6**, 3663 (2015).

[13] C. Motta, F. El-Mellouhi, S. Kais, N. Tabet, F. Alharbi, and S. Sanvito, Nature Comm. **6**, 7026 (2015).

[14] F. Zheng, L. Z. Tan, S. Liu, and A. M. Rappe, Nano Lett. **15**, 7794 (2015).

[15] J. M. Frost, K. T. Butler, F. Brivio, C. H. Hendon, M. van Schilfgaarde, and A. Walsh, Nano Lett. **14**, 2584 (2014).

[16] M. Kim, J. Im, A. J. Freeman, J. Ihm, and H. Jin, **111**, 6900 (2014).

[17] (), our implentation was adapted from the original ecalj code at `https://github.com/tkotani/ecalj`, and are available at `http://www.lmsuite.org/`.

[18] M. van Schilfgaarde, T. Kotani, and S. Faleev, Phys. Rev. Lett. **96**, 226402 (2006).

[19] A. N. Chantis, M. van Schilfgaarde, and T. Kotani, Phys. Rev. Lett. **96**, 086405 (2006).

[20] G. Lasher and F. Stern, Phys. Rev. **133**, A553 (1964).

[21] C. Barugkin, J. Cong, T. Duong, S. Rahman, H. T. Nguyen, D. Macdonald, T. P. White, and K. R. Catchpole, J. Phys. Chem. Lett. **6**, 767 (2015).

[22] A. Filippetti, P. Delugas, and A. Mattoni, J. Phys. Chem. C **118**, 24843 (2014).

[23] E. Kioupakis, Q. Yan, D. Steiauf, and C. G. V. de Walle, New J. Phys. **15**, 125006 (2013).

[24] R. L. Milot, G. E. Eperon, H. J. Snaith, M. B. Johnston, and L. M. Herz, Adv. Funct. Mater. **25**, 6218 (2015).

[25] T. Kotani and M. van Schilfgaarde, Phys. Rev. B **81**, 125201 (2010).

[26] M. B. Price, J. Butkus, T. C. Jellicoe, A. Sadhanala, A. Briane, J. E. Halpert, K. Broch, J. M. Hodgkiss, R. H. Friend, and F. Deschler, Nat. Commun. **6**, 8420 (2015).

[27] J. Even, L. Pedesseau, and C. Katan, J. Phys. Chem. C **118**, 11566 (2014).

[28] A. Miyata, A. Mitioglu, P. Plochocka, O. Portugall, J. T.-W. Wang, S. D. Stranks, H. J. Snaith, and R. J. Nicholas, Nat. Phys. **11**, 582 (2015).

[29] R. Del Sole and R. Girlanda, Phys. Rev. B **48**, 11789 (1993).

[30] See supplemental material at [URL will be inserted by AIP] for further technical details of the recombination rate model.

[31] T. Etienne, E. Mosconi, and F. D. Angelis, J. Phys. Chem. Lett. **7**, 1638 (2016), pMID: 27062910, http://dx.doi.org/10.1021/acs.jpclett.6b00564.

[32] G. E. Eperon, S. D. Stranks, C. Menelaou, M. B. Johnston, L. M. Herz, and H. J. Snaith, Energy Environ. Sci. **7**, 982 (2014).

[33] N. J. Jeon, J. H. Noh, W. S. Yang, Y. C. Kim, S. Ryu, J. Seo, and S. I. Seok, Nature **517**, 476 (2014).

[34] J. Ma and L. W. Wang, Nano Lett. **15**, 248 (2015).

[35] G. W. 't Hooft, Appl. Phys. Lett. **39**, 389 (1981).

[36] P. J. Bishop, M. E. Daniels, B. K. Ridley, and K. Woodbridge, Phys. Rev. B **45**, 6686 (1992).

[37] F. Stern, IEEE J. Quantum Electron. **9**, 290 (1973).

[38] C. H. Swartz, M. Edirisooriya, E. G. LeBlanc, O. C. Noriega, P. A. R. D. Jayathilaka, O. S. Ogedengbe, B. L. Hancock, M. Holtz, T. H. Myers, and K. N. Zaunbrecher, Appl. Phys. Lett. **105**, 222107 (2014).

[39] A. Kirk, M. DiNezza, S. Liu, X. H. Zhao, and Y. H. Zhang, in *Photovoltaic Specialists Conference (PVSC), 2013 IEEE 39th* (2013) pp. 2515–2517.

[40] X. H. Zhao, M. J. DiNezza, S. Liu, S. Lin, Y. Zhao, and Y. H. Zhang, J. Vac. Sci. Technolo. B **32**, 040601 (2014).

[41] T. Trupke, M. A. Green, P. Würfel, P. P. Altermatt, A. Wang, J. Zhao, and R. Corkish, J. Appl. Phys. **94**, 4930 (2003).

[42] W. Gerlach, H. Schlangenotto, and H. Maeder, Phys. Status Solidi (a) **13**, 277 (1972).

[43] The Fermi functions$f_c(1-f_v)$ are added to equation S1 due to the transition from a two-state single atom picture to band structure.

[44] Z. H. Levine and D. C. Allan, Phys. Rev. Lett. **63**, 1719 (1989).

[45] `http://www.lmsuite.org` (), accessed: 2016-04-01.

[46] P. E. Blöchl, O. Jepsen, and O. K. Andersen, Phys. Rev. B **49**, 16223 (1994).

[47] J. P. Perdew, A. Ruzsinszky, G. I. Csonka, O. A. Vydrov, G. E. Scuseria, L. A. Constantin, X. Zhou, and K. Burke, Phys. Rev. Lett. **100**, 136406 (2008).

[48] G. Kresse and J. Furthmüller, Phys. Rev. B **54**, 11169 (1996).

[49] `https://github.com/WMD-Bath/Hybrid-perovskites`, accessed: 2016-04-01.